Available online at www.sciencedirect.com
ScienceDirect
Acta Materialia 56 (2008) 2296–2306
Acta MATERIALIA
www.elsevier.com/locate/actamat

Incidence of nanoscale heterogeneity on the nanoindentation of a semicrystalline polymer: Experiments and modeling

F. Bédoui [a], F. Sansoz [b,*], N.S. Murthy [a]

[a] New Jersey Center for Biomaterials, Rutgers University, Piscataway, NJ 08854, USA
[b] School of Engineering and Materials Science Program, The University of Vermont, Burlington, VT 05405, USA

Received 17 November 2007; received in revised form 28 December 2007; accepted 14 January 2008
Available online 3 March 2008

Abstract

The nanoindentation of semicrystalline polyamide 6 (PA6) specimens was evaluated by atomic force microscopy with an extremely sharp diamond tip whose apex was nominally less than 10 nm in radius. Nanoindentation was performed under dry and wet conditions on PA6 samples injection-molded at different melt temperatures. The bulk Young's modulus of dry PA6 was found to be in good agreement with the literature, thereby confirming the experimental approach developed in this study. A major finding is the observation of sudden increases in force during the loading portion of the experimental load–displacement curves, which occurred regardless of water absorption. We also found some irregularity in the pile-up morphology around the indents, linked to the heterogeneous nature of the deformation in PA6. Finite element analysis was used to elucidate the phenomenon of force discontinuity by independently considering the variations in elasticity, yield stress and friction coefficient of the crystalline lamellar aggregates in PA6. It is shown that force discontinuities in nanoindented PA6 result from local differences in yield phenomena at the lamellar level. The present investigation sheds some light on the importance of mechanical heterogeneity emerging from contact interactions between an extremely sharp tip and the nanoscale morphology of semicrystalline polymers.

Keywords: Semicrystalline polymer; Yield phenomena; Nanoindentation; Atomic force microscopy; Finite element analysis

1. Introduction

Semicrystalline polymers, such as polyamide 6 (PA6), high-density polyethylene (HDPE) and isotactic polypropylene (iPP), are macromolecular materials consisting of nanoscale aggregates of folded-chain lamellar crystallites and intervening amorphous layers. Due to a wide range of structural applications using these polymers, there is a strong demand for determining their overall mechanical behavior based on the morphology and behavior of their underlying amorphous and crystalline constituents [1]. During processing, semicrystalline polymers are subjected to large plastic deformation, which results in the chains orienting preferentially, and gives rise to a high anisotropy in mechanical properties [1–3]. It is acknowledged that the elastic and plastic properties of the crystalline component and the symmetry of the lattice establish the final anisotropic properties of the material. As such, much of the previous understanding of deformation process in semicrystalline polymers has been obtained using macroscopic testing on highly oriented crystalline microstructures [4,5]. For example, Lin and Argon [4] have shown using uniaxial tension/compression experiments on textured PA6 that significant anisotropy in elastic stiffness and yield stress exists based on the crystal orientation.

With the advent of nanomechanical testing, nanoindentation techniques have provided new insights into the relevant length scale of deformation in semicrystalline polymers, because an indentation probe is very sensitive to the heterogeneous nature of the material being tested [6–10]. Nanoindentation has been used by Labour et al.

* Corresponding author.
E-mail address: frederic.sansoz@uvm.edu (F. Sansoz).

1359-6454/$34.00 © 2008 Acta Materialia Inc. Published by Elsevier Ltd. All rights reserved.
doi:10.1016/j.actamat.2008.01.021

[11] to determine two distinctive sets of elastic modulus and hardness corresponding to the α and β crystalline forms of spherulites in iPP. This technique has also been used successfully on annealed PA6 specimens obtained from compression molding and injection molding [12,13]. In particular, the nanoindentation study of Shen et al. [13] has clearly shown the occurrence of heterogeneity in elastic modulus and hardness in PA6, for which case the α-form crystal was found to exhibit significantly higher stiffness and hardness than the γ-form crystal. Despite such insights, it must also be recognized that some significant challenges still exist in the interpretation of micro/nanoindentation data on semicrystalline polymers. For example, Gourrier et al. [14] have shown for different bulk semicrystalline polymers that the process of microindentation leads to local crystalline reorientation. The reorientation of crystalline aggregates directly relates to the volume of materials being plastically deformed by the tip which, in the above study, was much larger than the size of individual aggregates. Using atomic force microscopy (AFM) with a Berkovich-like diamond tip mounted on a stainless steel cantilever, Du et al. [15] have also concluded that for highly oriented HDPE films the anisotropy in elastic modulus at the lamella level causes an apparent increase in bulk elastic modulus determined from nanoindentation. Clearly, these results support the idea that the nanoindentation process must be further refined in order to better characterize the impact of nanoscale heterogeneity on the mechanical response of semicrystalline polymers.

AFM is a technique commonly used for nanoscale imaging of surfaces [16–18]. Recent progress in the fabrication of metrology scanners and diamond-tipped AFM cantilevers, and the refinement of current calibration methods, has made it possible to improve the accuracy of this instrument for the nanomechanical characterization of hard and soft materials using nanoindentation [7,8,19–25]. In AFM-based nanoindentation, extremely sharp tips can be mounted on specialty cantilevers, which enable smaller volumes of materials to be probed than with other instrumented nanoindentation techniques. Recently, meaningful results on the role of nanoscale heterogeneity on the mechanical properties of bone, an example of a hierarchically structured material, have been successfully evidenced by this technique [26]. Tranchida et al. [25] have also confirmed that AFM nanoindentation makes it possible to characterize the mechanical behavior of polymers on an unparalleled small scale compared to commercial depth-sensing instruments, which use a much blunter indenter.

The purpose of the present research was to use AFM-based nanoindentation in order to shed light on the contact interactions between an extremely sharp diamond tip and the nanoscale morphology of a model semicrystalline polymer. Section 2 describes the experimental procedure aimed at the material preparation and nanoindentation using the AFM with an ultrasharp diamond tip whose apex was nominally less than 10 nm in radius of curvature. In Section 3, we present the results of AFM-based nanoindentation experiments carried out on injection-molded PA6 obtained from different melt temperatures and under both dry and wet conditions. Using this technique, we show direct evidence of an unusual load–displacement response characterized by sudden increases in force during the loading portion of the load–displacement nanoindentation curves. Such force discontinuities are thought to correspond to the interaction of the tip with nanoscale lamellar aggregates. In Section 4, we use a finite element analysis (FEA) to confirm this hypothesis by modeling several cases involving different elastic, plastic and friction properties in the lamellar aggregates. Finally, the factors influencing the force discontinuity phenomenon are discussed in Section 5 in light of both experimental and modeling results.

2. Experimental details

Unfilled, heat-stabilized PA6 samples (Honeywell International, Capron 8202, $M_w = 22{,}900\ \mathrm{g\ mol^{-1}}$) were injection-molded at different melt temperatures (225, 235, 260, 270, 290 and 310 °C). The samples were mechanically polished on sandpaper up to 1200 grit, and ultrasonically cleaned in ethanol to achieve a smooth topographical profile. Dry specimens were obtained by maintaining the materials for at least 2 h under high vacuum. Wet specimens were prepared by immersing the samples for 16 h in water. No thick water film was present at the surface of the wet specimens.

AFM imaging and nanoindentation were performed simultaneously using a universal scanning probe microscope (Quesant, Santa Cruz, CA). The principle of the nanomechanical characterization of semicrystalline PA6 samples by nanoindenting AFM is schematically represented in Fig. 1a. In order to improve the spatial resolution of the probe positioning, a metrology-enabled scanner, which consisted of capacitive sensors measuring the three-dimensional position of the scanner, was added to the system. Following the manufacturer's calibration procedure, scanner positioning precisions of 0.86 and 0.40 nm were achieved along the XY and Z directions, respectively. A diamond-tipped sapphire AFM cantilever (Micro-Star Technologies, Huntsville, TX), shown in Fig. 1b, was used to concurrently perform AFM topography imaging and nanoindentation of the PA6 samples. The tip geometry consisted of a sharp three-sided pyramid with total included angle of 39° (angle from one edge to the opposite side) and half-angle of 13° (Fig. 1c). A 12° tilt compensation angle was added to the tip to make the indentation normal to the surface of the sample. The dimensions of the cantilever were determined by scanning electron microscopy (SEM) (JEOL JSM6060). The radius of curvature at the tip apex was nominally less than 10 nm (based on the manufacturer). However, a caveat here is that no precise method exists to characterize the tip geometry at such a small scale. All nanoindentation was carried out on the core of the material. At least three nanoindentation tests were performed at different locations

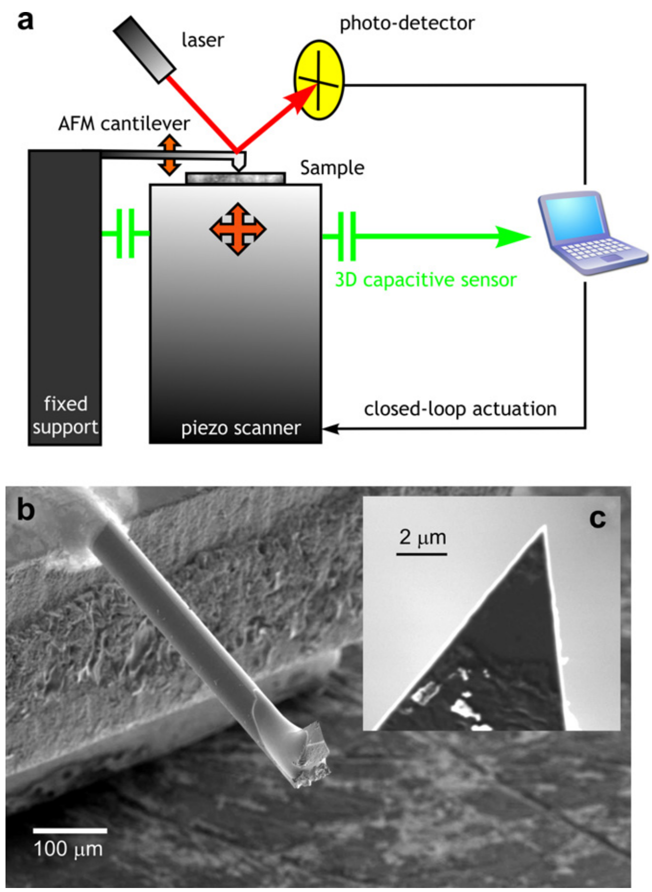

Fig. 1. Nanomechanical characterization of semicrystalline polyamide 6 (PA6) samples by nanoindenting atomic force microscopy (AFM). (a) Schematic representation of the AFM set-up. (b) SEM image of the diamond-tipped AFM sapphire cantilever. (b) Close-up of the side of the pyramidal tip.

on the sample for a given test condition. The residual indentation area was measured at the end of the test by tapping-mode topography AFM imaging and analyzed numerically by a scanning probe image processor (Image Metrology, Hørsholm, Denmark). The cantilever deflection was obtained by the output voltage of the laser reflection on the AFM photodetector. A linear relation between measured voltage and cantilever deflection was determined and calibrated before each test by elastically indenting the surface of a polished fused-quartz sample (GoodFellow, Oakdale, PA) using a small force (<10 μN). The indentation depth in the polymeric samples was calculated by subtracting the actual cantilever deflection from the sample displacement measured by the metrology scanner. Error in force measurement often depends on the method used to calibrate the AFM's cantilever force constant [27–31]. The AFM cantilever force constant K_z is defined by

$$F = K_z \cdot \delta, \tag{1}$$

where F is the contact force normal to the surface and δ is the cantilever deflection. In this study, we used a dynamic calibration method in air for its simplicity and accuracy [31]. Assuming only one vibration mode, K_z given by this method is

$$K_z = \frac{12}{\alpha_1^4} \rho w t L (\pi f_r)^2, \tag{2}$$

where ρ, t, w and L denote the density, thickness, width and length of the cantilever, respectively. α_1 is a dimensionless constant relative to the first vibration mode (=1.88) [27], and f_r is the resonant frequency of the probe, which was determined prior to the test. Using $\rho = 3980\ \mathrm{kg\ m^{-3}}$ for sapphire, and $t = 32\ \mu\mathrm{m}$, $w = 55.5\ \mu\mathrm{m}$, $L = 535\ \mu\mathrm{m}$ and $f_r = 119\ \mathrm{kHz}$ from our measurements, the cantilever spring constant K_z was found to be equal to $503\ \mathrm{N\ m^{-1}}$, which was in excellent agreement with the manufacturer's specification. Nanoindentation measurements were carried out up to a maximum load of 120 μN, followed by an unloading. The loading and unloading rates were approximately kept constant (~4 $\mu\mathrm{N\ s^{-1}}$). No hold time at maximum load was applied before unloading.

The bulk elastic modulus of the PA6 samples was determined by measuring the effective elastic modulus E^* defined by [32]

$$\frac{1}{E^*} = \frac{1 - \nu_{\mathrm{sample}}^2}{E_{\mathrm{sample}}} + \frac{1 - \nu_{\mathrm{tip}}^2}{E_{\mathrm{tip}}}, \tag{3}$$

where the elastic modulus (E_{tip}) and Poisson's ratio (ν_{tip}) of the diamond tip were taken as 1070 GPa and 0.07, respectively [32]. The Poisson's ratio of the PA6 samples (ν_{sample}) was assumed to be constant (~0.46 [33]) under all conditions. The value of E^* was determined using the Oliver–Pharr [34] method for pyramidal nanoindentation by the equation

$$E^* = \frac{\sqrt{\pi}}{2\beta} \frac{S_{\max}}{\sqrt{A}}. \tag{4}$$

In this expression, $S_{\max} = \mathrm{d}F/\mathrm{d}h|_{F=F\max}$ is the contact stiffness measured at the unloading. β is a geometrical correction factor (1.05 for a three-sided pyramidal tip) [34], and A is the residual indentation area, which was measured at the end of the test by AFM imaging. We also used the reference fused-quartz sample to calibrate a shape function for the calculation of the elastic moduli at deep indentation depths (>50 nm) from Eq. (4). No elastic modulus measurements have been performed for shallow indentations (<50 nm) due to the large uncertainty in the tip geometry at such a small scale.

3. Results from AFM-based nanoindentation

The AFM images of the residual impression left on a dry PA6 sample are presented in Fig. 2. This figure shows that the material did undergo notable plastic deformation during indentation. Significant pile-up of material was also observed around the indent. It is worth noting that the appearance of such pile-up was found to be irregular, as opposed to a smooth, clean surface. This result is some-

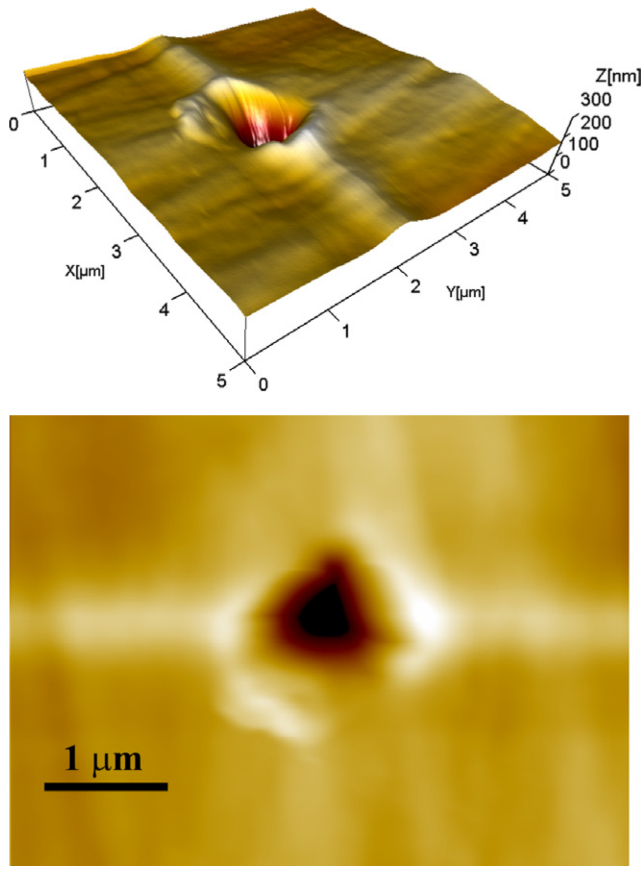

Fig. 2. Tapping-mode topographical AFM images of the residual impression on dry PA6 for a nanoindentation load of 120 µN. Note the irregularity of the pile-up morphology around the indent.

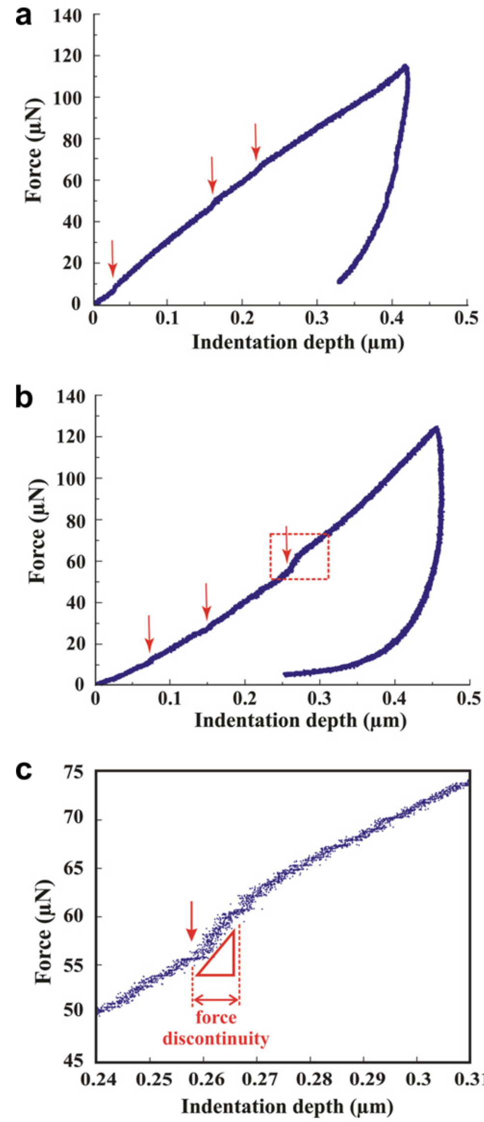

Fig. 3. Representative load–displacement curves on (a) dry and (b) wet PA6. Arrows indicate the onset of force discontinuity effects observed during the loading portion of the nanoindentation. (c) Close-up on a force discontinuity in wet PA6 corresponding to the dashed area in (b).

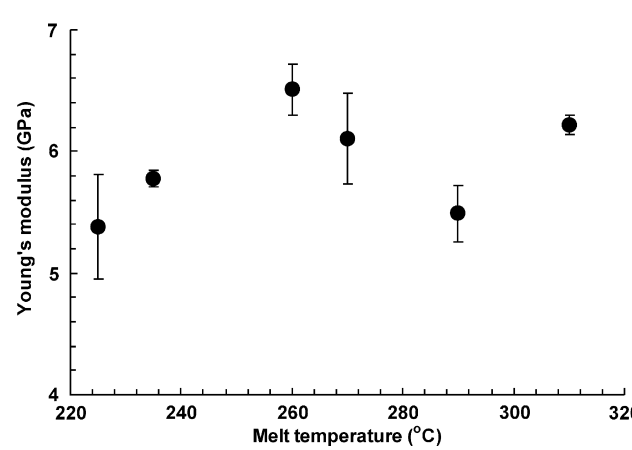

Fig. 4. Bulk elastic modulus of dry PA6 determined from AFM-based nanoindentation as a function of melt temperature.

what reminiscent of the distorted pile-up observed around indents of some metallic alloys due to the inhomogeneity of their structure [35]. Fig. 3 gives the representative load–displacement curve of nanoindented PA6 samples obtained under dry and wet conditions. The contact stiffness S_{max} used in Eq. (3) was determined from the slope of the nanoindentation curve by fitting a line to the initial portion of the unloading curve. Fig. 3b shows that the slope of the unloading curve was largely negative under wet conditions as opposed to that in dry samples. This observation suggested that water absorption caused PA6 to creep significantly during nanoindentation [36]. Therefore, Eq. (3) could not be used to determine the elastic modulus of wet PA6 samples from nanoindentation. The bulk elastic modulus for dry PA6 samples, as obtained from Eqs. (3) and (4), was found to vary from 5.12 to 5.92 GPa as shown in Fig. 4. These results were in good agreement with the elastic moduli of oriented capron 8200 PA6, which are 6.2 and 4.3–3.6 GPa along the longitudinal and transverse directions of the crystalline lamellae, respectively, as measured from uniaxial compression experiments by Lin and Argon [4].

Furthermore, the nanoindentation response of PA6 revealed multiple sudden increases in force, referred to as force discontinuities in the following, at different indentation depths. Several force discontinuities are indicated by arrows in Fig. 3. Such discontinuities were predominantly seen during the loading portion of the nanoindentation curve and only sometimes during unloading. Similar force discontinuities have been observed previously during nanoindentation of nanocrystalline copper thin films and were interpreted as discontinuous deformation events [37]. A close-up of a force discontinuity is shown in Fig. 3c. In this example, the slope variation between the start and end of the force discontinuity occurred over a penetration depth of 10 nm. It is shown below from our FEA modeling that the change in slope presented in Fig. 3c should be interpreted as a discontinuity of force related to an abrupt change in contact area, as opposed to two displacement discontinuities very close to each other. It is also important to note that the number of force discontinuities varied from one test to the other and their magnitude changed for the same test. This effect was observed in all our samples, regardless of the melt temperature and whether the sample was wet or dry. This last observation, coupled to the heterogeneous nature of the deformation, suggested that the occurrence of force discontinuities was related to the properties of the crystalline lamellar aggregates, because it is known that moisture influences the properties of the amorphous phase without affecting those of the crystalline phase in PA6 [38].

4. Finite element analysis

4.1. Modeling procedure

FEA was used to investigate the origin of force discontinuities observed during the loading portion of the nanoindentation experiments on PA6. A two-dimensional axisymmetric model corresponding to the conical indentation of a polymer substrate was created using standard FEA software (ABAQUS, Inc.). The FEA mesh used for this study was created using linear quadrilateral elements as shown in Fig. 5. Mesh refinement was performed in the contact region with 26.0 nm × 24.8 nm elements. The nodes at the bottom of the mesh were fixed along both vertical and horizontal directions. The nodes lying on the symmetry axis of the mesh were only free to move vertically. The indenter was modeled as an analytical rigid surface with a cone angle of 44.7° and a tip radius of 25 nm, similar to the size of the smallest finite element in the model. The cone angle was determined based on the equivalent projected contact area obtained from imaging of the impressions left by the pyramidal tip after testing. The contact behavior at the tip–substrate interface was modeled using a friction coefficient of $\mu_1 = 0.05$. The rigid indenter was statically displaced downward in steps equal or smaller than 4 nm, up to a depth of 400 nm. An implicit integration solver was used for the static treatment. Furthermore, the model was divided into a homogeneous substrate region and a heterogeneous contact region (Fig. 5), as described below.

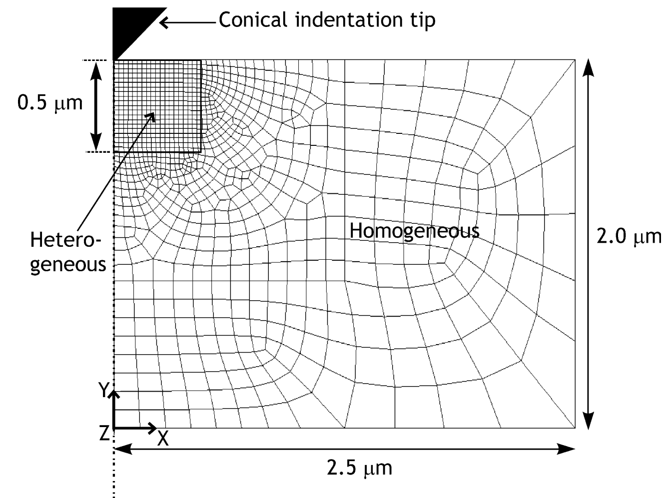

Fig. 5. Two-dimensional axisymmetric mesh used for the finite element analysis (FEA) of conical nanoindentation of PA6. The continuum model is divided into a region of homogeneous deformation, and a contact region with heterogeneous deformation due to nanoscale aggregates with different elastic–plastic properties. The conical indenter tip is assumed to be perfectly rigid.

The homogeneous region was uniformly assigned an elastic–perfectly plastic behavior with isotropic yielding. The bulk elastic properties and density of this region are given in the right column of Table 1. The yield stress used for the simulation was determined by fitting the simulated nanoindentation curve to the experimental data on dry PA6 (Fig. 3a), assuming that the substrate was fully homogeneous with an initially elastic, then perfectly plastic behavior. A yield stress of $Y = 70$ MPa was found to best approximate the experimental load–displacement curve. This value was in agreement with the yield stress found in compression on oriented nylon 6 [4], which is in the range of 38–78 MPa based on the slip system and crystal orientation with respect to the loading direction. The fact that the simulated value is near the upper limit of this range can be attributed to the small discrepancy in geometry between simulated and actual AFM tips and, specifically, the tip radius for shallow nanoindentation [39].

Table 1
Bulk elastic properties and densities used in the FEA model

	α-Form crystal of PA6	Homogeneous PA6
C_{11}	312.950 (GPa)	–
C_{22}	3.75734 (GPa)	–
C_{33}	11.6769 (GPa)	–
C_{12}	1.28867 (GPa)	–
C_{13}	1.50990 (GPa)	–
C_{23}	3.66399 (GPa)	–
C_{44}	2.43724 (GPa)	–
C_{55}	0.85244 (GPa)	–
C_{66}	2.38379 (GPa)	–
ρ (kg m^{-3})	1165	1128
E (GPa)	–	5.0
ν	–	0.46

The heterogeneous region was used to locally give different mechanical properties to a lamellar aggregate embedded into the homogeneous matrix. The top side of the aggregate was exposed to the free surface in order to enable direct contact between the tip of the indenter and the aggregate during penetration. In this study, the simulated lamellar aggregate represented a nanosized domain where the crystalline phase had a preferential texture and strong mechanical anisotropy. The modeled lamellar aggregate had an arbitrary ring shape with rectangular cross-sectional area (225 nm × 300 nm) whose axis coincided with the axisymmetry axis. The shape of the aggregate was chosen to enable the two-dimensional axisymmetry assumption, which greatly reduced the computational requirements. The inner and outer radii of the lamellar aggregate were chosen as 50 nm and 275 nm, respectively, except where otherwise noted. Local variations in elastic anisotropy, friction and yield stress caused by the mechanical anisotropy of the aggregate were separately considered.

4.2. Effect of elastic anisotropy of lamellar aggregates

Fig. 6 represents the effect of elastic anisotropy of the lamellar aggregate on the simulated load–displacement curve of PA6. To achieve the results shown in this figure, we used the stiffness constants of the α-form of PA6 crystals, as theoretically predicted by Tashiro and Tadokoro [4,40], which are recalled in the left column of Table 1. The elastic behavior of PA6 is considered to be orthotropic because, in crystalline PA6 aggregates, the material can be stiffer by more than one order of magnitude along the longitudinal direction of the lamellae than the transverse directions [41]. We studied three in-plane rotations of the crystal structure corresponding to $\theta = 0°$, 45° and 90° where θ represents the angle between the longitudinal direction of the lamellae (direction 1 in Fig. 6) and the horizontal axis. In addition, both heterogeneous and homogeneous regions were assumed to have identical friction and yield stress properties for these calculations. We also simulated the case where the substrate contained no lamellar aggregate and was fully isotropic. Fig. 6 clearly shows that there is no significant effect of the elastic anisotropy of the crystalline phase on the loading portion of the nanoindentation response of PA6.

4.3. Effect of interface friction

Earlier studies on the wear of PA6 [42] have also shown that the coefficient of friction of this material could significantly increase up to a value of 0.7. Furthermore, it is acknowledged that friction effects at the indenter tip–substrate interface become significant when the tip geometry is sharp [43]. Therefore, we used our FEA model to vary only the coefficient of friction (μ_2) along the free surface of the aggregate while keeping all other properties constant. Fig. 7 represents the effect of local variations in friction force at the tip–aggregate interface in nanoindented PA6. We observed some change in the nanoindentation curve with small variations in interface friction. Such change was characterized in Fig. 7 by small force fluctuations occurring for penetration depths between 120 and 320 nm. However, we also observed that there was no significant increase in the magnitude of these fluctuations as the coefficient of friction of the lamellar aggregate increases, up to a value of 0.7.

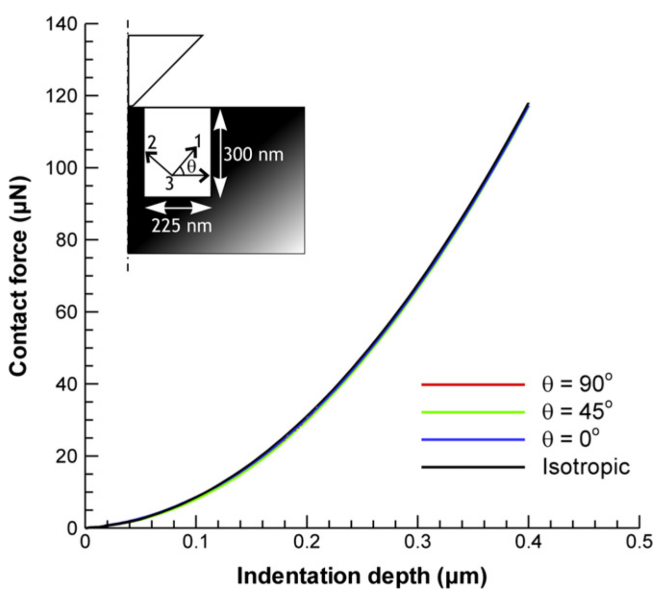

Fig. 6. Simulated load–displacement curves on PA6 containing one lamellar aggregate (225 nm × 300 nm) with large anisotropy in elastic stiffness and same yield stress ($Y = 70$ MPa) than that of the homogeneous matrix. The crystal orientation is represented by the angle θ formed by the longitudinal axis of the lamellae (axis 1) with respect to the horizontal axis.

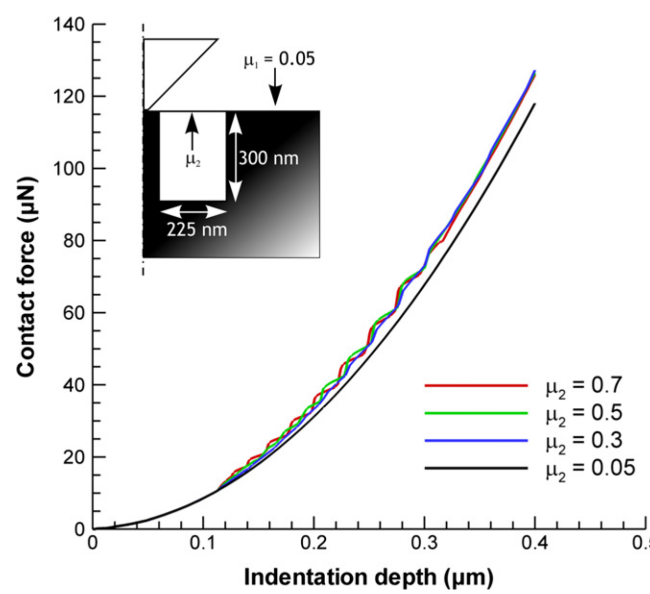

Fig. 7. Simulated load–displacement curves on PA6 containing one lamellar aggregate (225 nm × 300 nm) with different coefficient of friction (μ_2) than that of the matrix ($\mu_1 = 0.05$).

4.4. Effect of yield stress of lamellar aggregates

Lin and Argon [4] have obtained detailed measurements of the plastic anisotropy of oriented PA6 to establish that there could be a 2-fold increase in the crystallographic slip process and yield stress in compression from the (001) [010] slip system and the (100) [010] slip system. In this section, we therefore investigate the situation where the nanoindentation tip would encounter lamellar aggregates oriented along the direction that yields to the largest slip resistance. Fig. 8a represents the simulated load–displacement curves on PA6 with uniform elastic and friction properties, but a difference of yield stress between the matrix and the lamellar aggregate. In this figure, Y_1 and Y_2 are the yield stress values for the matrix and lamellar aggregates, respectively. It is worth noting that the plastic yield phenomenon was considered at the lamellar aggregate scale rather than at the single-crystal one, using an isotropic yielding. Fig. 8a shows that the slope of the nanoindentation curves increased gradually at a penetration depth of 50 nm, as the yield stress of the lamellar aggregate was varied from the yield stress in the matrix ($Y_2 = Y_1 = 70$ MPa) to more than twice this value ($Y_2 = 150$ MPa). The change in slope was observed when the first portion of the tip was brought into contact with the surface of the aggregate. A force discontinuity was also found for a penetration depth of 300 nm, which occurred after the tip was fully in contact with the surface of the aggregate, as indicated by an arrow in Fig. 8a. It should also be noted that the magnitude of the discontinuity increased with the increase in yield stress in the lamellar aggregate. Small fluctuations in force were observed after the discontinuity, but to a lesser extent than the fluctuations described above when only the friction coefficient of the lamellar aggregates was varied.

Furthermore, we investigated the effect of the thickness of the aggregate on the occurrence of the force discontinuity. To accomplish this task, we decreased the lateral dimension of the aggregate from 225 to 75 nm, while imposing a large difference in yield stress between the matrix and the aggregate (i.e. $Y_1 = 70$ MPa and $Y_2 = 150$ MPa). In addition, we varied the position (X) of the new aggregate with respect to the symmetry axis. Fig. 8b shows that the penetration depth, at which the force discontinuity occurs, is correlated to the position of a 75 nm thick lamellar aggregate. However, it is also important to note that the thickness of the lamellar aggregate does not influence the magnitude of the force discontinuity. The latter is clearly demonstrated by the fact that the nanoindentation curve of a 75 nm thick lamellar aggregate at position $X = 200$ (Fig. 8b) is identical to that for a 225 nm thick aggregate with a yield stress of $Y_2 = 150$ MPa (Fig. 8a). The penetration depth, at which the tip is fully in contact with the surface of the lamellar aggregate, was also indicated for comparison. The latter suggested that the force discontinuity always appeared after full contact between tip and aggregate had been made.

To better understand the above results, we also compared the difference in pile-up morphology around the indent between a fully homogeneous material and one consisting of nanoscale heterogeneity in yield stress, since the AFM nanoindentation experiments showed that the surface of the pile-up appeared to be irregular. Fig. 9 represents several steps of deformation near the tip/matrix contact region for these two cases obtained from FEA. It is worth mentioning that in these nanoindentation simulations, PA6 was treated as a two-phase continuum model with the largest difference in yield stress investigated in this study (i.e. $Y_1 = 70$ MPa and $Y_2 = 150$ MPa). Fig. 9a–d

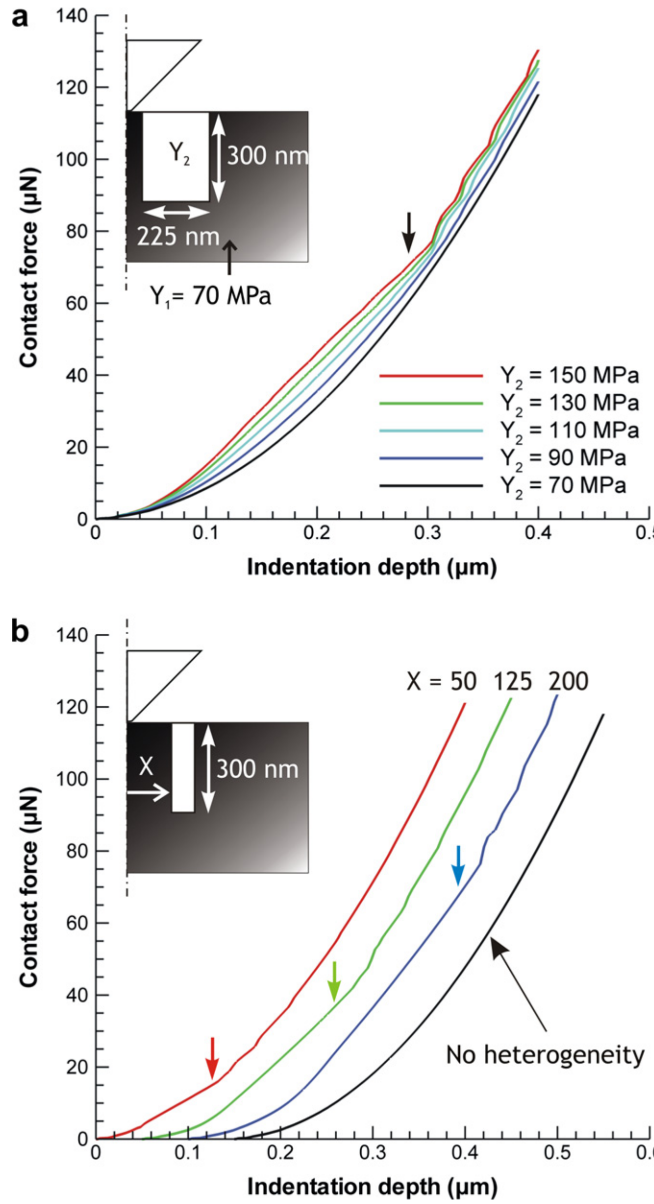

Fig. 8. Simulated load–displacement curves of PA6 with uniform elastic properties and local variations in yield stress. (a) FEA model consisting of one lamellar aggregate (225 nm × 300 nm) with different values of yield stress (Y_2) as indicated ($Y_1 = 70$ MPa). (b) FEA model consisting of a smaller lamellar aggregate (75 nm × 300 nm) with large yield stress ($Y_2 = 150$ MPa) at different positions (X) from the symmetry axis. X is in units of nm. The arrows show the penetration depth at which the tip is fully in contact with the surface of the lamellar aggregate. In (b), the curves have been shifted to the right for clarity.

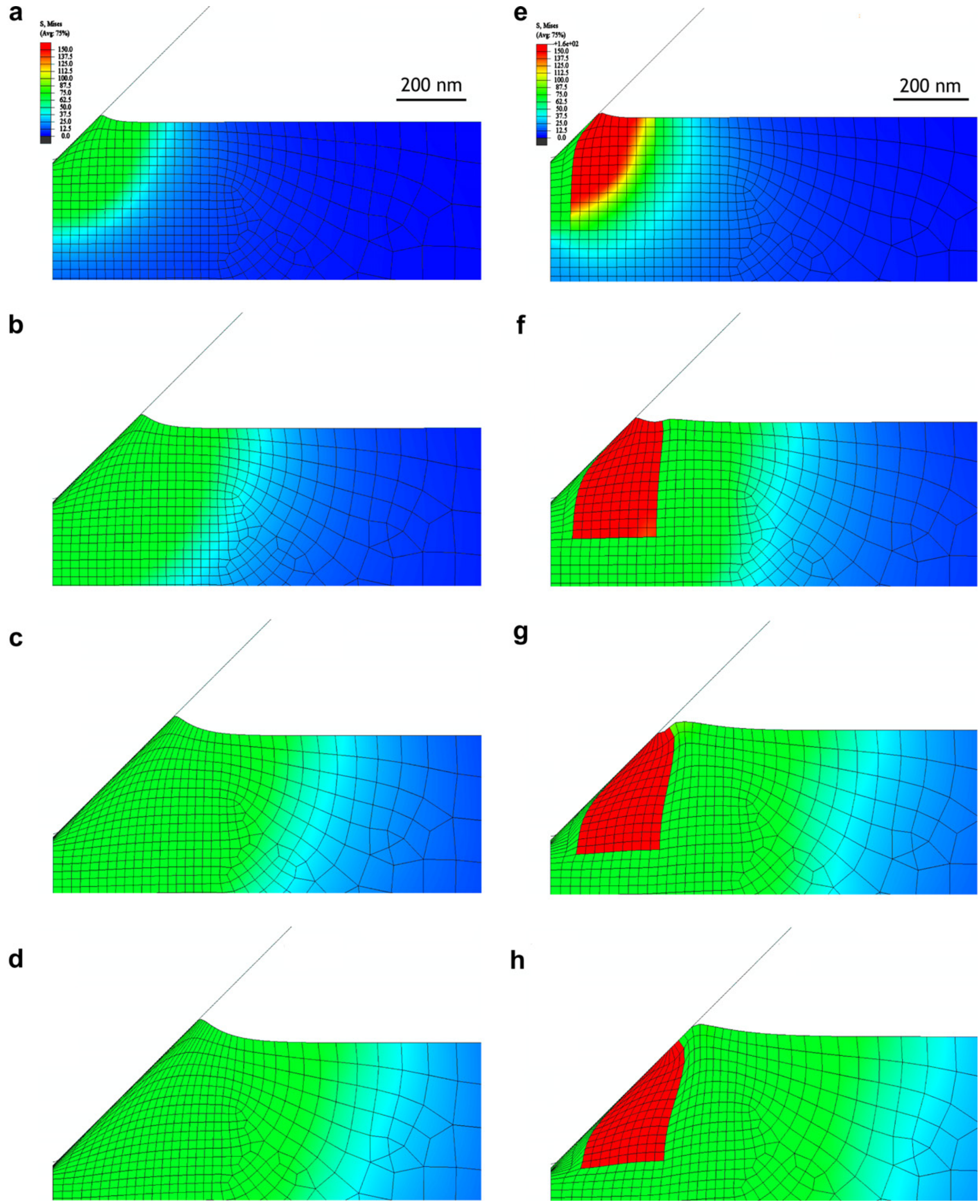

Fig. 9. Pile-up morphology around the tip during nanoindentation of PA6 simulated as a two-phase continuum model from FEA. The contours represent the change in the equivalent von-Mises stress for matrix and lamellar aggregate with (a)–(d) having the same elastic–plastic behavior and (e)–(h) the same elastic behavior but different yield stress ($Y_2 = 150$ MPa, $Y_1 = 70$ MPa). Double pile-up effect and abrupt change in contact area appear in (f) and (h), respectively.

represents the sequence of deformation for a fully homogeneous material. This sequence shows that the pile-up around the indent has a shape similar to that simulated by others using FEA on two-phase materials with uniform properties [44]. In contrast, Fig. 9e–h shows that the deformation around the indent forms two pile-ups in the presence of a lamellar aggregate. More specifically, Fig. 9f shows two separate pile-ups formed simultaneously in both lamellar aggregate and at the matrix/aggregate interface. In this figure, it appears that the formation of the second pile-up at the matrix/aggregate interface is due to the compression of the lamellar aggregate against the softer matrix.

It can also be seen in Fig. 9h that only one pile-up remained after the tip was fully brought in contact with the surface of the aggregate, which corresponds to an abrupt change in contact area.

5. Discussion

The ultimate goal of the present study was to investigate the effects of plasticity confinement on the mechanical properties of a model semicrystalline polymer using sharp tip nanoindentation. The AFM-based nanoindentation procedure used herein to accomplish this task is validated by the results of bulk elastic modulus obtained on dry PA6 as shown in Fig. 4. In particular, the values of elastic modulus determined under dry conditions are in good agreement with earlier reports on this material [4].

A salient feature of our AFM experiments is the occurrence of force discontinuities during the loading portion of the load–displacement curves. The force discontinuity effects were found to occur regardless of water absorption. It is known that water affects the properties of the amorphous regions without affecting those of the crystalline phase [38]. This observation therefore suggests that force discontinuity phenomena are related to the latter. Since our PA6 samples were injection-molded, a spherulitic structure made of aggregates of lamellae is expected in the core [2]. The chain-axes of the crystals in these lamellar aggregates are all normal to the radii. The length of the lamellae can approach the spherulite radii (4–13 μm) [2]. We therefore propose to explain the sharp increase in force along the load–displacement curves of nanoindented PA6 by considering both anisotropy and inhomogeneity in properties at the lamellar level.

To address the above aspect, we first consider the variations in friction force that could possibly exist at the interface between the tip and the surface of the lamellar aggregate. In Fig. 7, FEA simulations show that some force fluctuations can result from the difference in friction coefficient between matrix and aggregate. These force fluctuations occurred from the very beginning of the contact between tip and lamellar aggregate, over the entire length of the aggregate (~225 nm), thus providing some support for the idea that they also depend on the thickness of the lamellar aggregate. In contrast, the experimental data in Fig. 3c shows that the increase in force during the loading portion of the load–displacement curve is infrequent and spans a very short penetration depth (~10 nm), which is much smaller relative to the size of actual lamellar aggregates in PA6 (>100 nm). We can therefore conclude that force discontinuity effects in the load–displacement curves cannot be fully explained by the variations in friction coefficient between the matrix and the lamellar aggregates.

A better way to interpret the force discontinuity phenomena is by considering the anisotropy in mechanical behavior of the lamellar aggregates. This hypothesis is supported by the large degree of irregularity of the pile-up morphology found around the indents, which is somewhat reminiscent of the distorted pile-up observed around indents of some metallic alloys caused by the inhomogeneity of their structure [35]. The orientation of the crystalline lamellae is known to be a major factor causing mechanical anisotropy in the elastic and plastic behavior of PA6 [4]. While the elastic modulus of the PA6 amorphous phase can be considered isotropic, with typical values ranging from 0.7 to 2.34 GPa [41], the modulus of the crystals is strongly anisotropic. In particular, the modulus of the lamellae along the chain direction was found to be of the order of 183 GPa from X-ray measurements, although the theoretical values are as high as 262 GPa [45]. In the plane of the hydrogen-bonded sheets, the modulus is about 15 GPa, whereas in the direction normal to the sheets, governed by van der Waals interactions, the modulus drops to 7 GPa [41]. However, the FEA results presented in Fig. 6 clearly indicate that the elastic anisotropy of the PA6 lamellar aggregates has no significant effect on the load–displacement curves. This conclusion is indeed consistent with the fact that for sharp tip geometries, load–displacement nanoindentation curves are more significantly sensitive to variations in yield stress and strain-hardening parameters of the material than to variations in Young's modulus [46].

Furthermore, as mentioned above, Lin and Argon [4] have postulated dislocation plasticity at the edges of lamellae in semicrystalline polymers. In particular, they were able to establish in oriented PA6 that a 2-fold increase in the slip resistance and yield stress exists in compression between the (0 0 1) [0 1 0] slip system and the (1 0 0) [0 1 0] slip system. We have also shown in Fig. 8a using FEA that a 2-fold difference in yield stress between matrix and lamellar aggregate caused a notable discontinuity in the slope of the load–displacement curve. Therefore, the force discontinuities observed during AFM-based nanoindentation experiments could result from the interaction of the tip with lamellar aggregates oriented along the direction that yields to the largest slip resistance. This effect may be found to be more acute with AFM-based nanoindentation than with other nanoindentation techniques, because the tip is much sharper and more likely sensitive to the orientation of the PA6 lamellar aggregates. Despite the fact that a single-crystal plasticity model has not been used in our computational analysis, the FEA confirms that the magnitude of the discontinuity is strongly dependent upon the difference in yield phenomena between the matrix and the aggregate. From a mechanistic viewpoint, the FEA model suggests that the increase in force during the loading portion of the load–displacement curve corresponds to the formation of a double pile-up around the indent and an abrupt increase in contact area. Fig. 9f shows that the formation of the second pile-up at the matrix/aggregate interface is due to the compression of the hard lamellar aggregate against the softer matrix. It can also be seen in Fig. 9h that only one pile-up remained after the tip was fully brought in contact with the surface of the aggregate. One force discontinuity can therefore be viewed as resulting from the increase of contact area occurring when, in turn, the second pile-up at the matrix/aggregate interface touches the surface of the tip as shown in Fig. 9h. This hypothesis is also supported by the FEA predictions, which show that force discontinuities do not depend on the thickness of the aggregate, and only occur after the tip and the aggregate are fully in contact, as shown in Fig. 8b.

Based on our FEA modeling, the slope variation found in the load–displacement curve in Fig. 3c can be interpreted as a discontinuity in the force related to an abrupt change in contact area after the tip encounters a crystalline lamellar aggregate with the highest slip resistance. The observed "force jump" phenomenon is somewhat reminiscent of the staircase yielding effect described by Cordill et al. [47]. The staircase yielding mechanism results from displacement discontinuities occurring in the contact area of the indenter due to the burst of dislocations at a critical load. In such case, each dislocation event is followed by an abrupt change in contact area until the next dislocation event, which results in a steeper slope in the nanoindentation curve. Similarly, in nanoindented semicrystalline PA6, this study demonstrates that the slope variations in the load–displacement curve occurred after the lamellae were fully plastically deformed, rather than at the onset of yielding, due to the discontinuous increase in contact area around the indenter.

6. Conclusions

The nanoindentation of semicrystalline PA6 specimens under dry and wet conditions was investigated by AFM using an extremely sharp diamond tip whose apex was nominally less than 10 nm in radius. Two-dimensional axisymmetric FEA was also performed to simulate the deformation by a rigid conical indenter of a PA6 substrate consisting of heterogeneous lamellar aggregates. The conclusions of this work can be summarized as follows:

- AFM-based nanoindentation on semicrystalline PA6 enables the bulk elastic modulus of the polymer to be determined under dry conditions. The results are in good agreement with earlier reports on capron 8200 PA6 obtained from uniaxial deformation.
- A salient feature of our AFM experiments is the occurrence of force discontinuity effects corresponding to sharp increases in force along the load–displacement curves of nanoindented PA6. The force discontinuities were found to occur regardless of water absorption. Furthermore, it was found that the surface morphology of the plastic pile-ups left around the indents was irregular. These two observations suggest that the occurrence of force discontinuities in nanoindented PA6 is related to local variations and anisotropy in the properties of the crystalline lamellar aggregates.
- It was shown by FEA that force discontinuity effects during indentation directly arise from the variations in yield phenomena at the lamellar level. Such phenomena could result from the interaction of the tip, with lamellar aggregates oriented along the direction that yields to the largest slip resistance. The elastic anisotropy of the aggregate was found to have no influence and the effect of the change in friction coefficient was negligible. The FEA also indicated that the force discontinuity effects depend on the position, rather than the thickness, of the lamellar aggregate with respect to the indenting tip.
- Microscopically, the FEA suggests that the sharp increase of force in the load–displacement curves corresponds to the formation of a double pile-up around the indent due to the compression of hard lamellar aggregates against the softer matrix. Force discontinuity effects can therefore be interpreted by considering the abrupt increase of contact area occurring around the indenter.

The present investigation reveals the importance of mechanical heterogeneity emerging from contact interactions between an extremely sharp tip and the nanoscale morphology of semicrystalline polymers.

Acknowledgement

N.S.M. and F.B. acknowledge support from NSF grant DMR-0513926. F.S. acknowledges support from Vermont Experimental Program to Stimulate Competitive Research (VT EPSCoR) under grant number NSF EPS 0236976, and the Outwater Funding Award at the University of Vermont. We also thank the reviewer for providing some useful comments on the interpretation of force discontinuities in nanoindentation experiments.

References

[1] van Dommelen JAW, Parks DM, Boyce MC, Brekelmans WAM, Baaijens FPT. J Mech Phys Solids 2003;51:519.
[2] Galeski A, Argon AS, Cohen RE. Macromolecules 1988;21:2761.
[3] Su KH, Lin JH, Lin CC. J Mater Process Technol 2007;192–193:532.
[4] Lin L, Argon AS. Macromolecules 1992;25:4011.
[5] Dencheva N, Denchev Z, Jovita Oliveira M, Funari SS. J Appl Polym Sci 2007;103:2242.
[6] Briscoe BJ, Fiori L, Pelillo E. J Phys D: Appl Phys 1998;31:2395.
[7] Reynaud C, Sommier F, Quet C, El Bounia N, Due TM. Surf Interface Anal 2000;30:185.
[8] VanLandingham MR, Villarrubia JS, Guthrie WF, Meyers GF. Macromol Symp 2001;167:15.
[9] Shen YL, Guo YL. Model Simul Mater Sci Eng 2001;9:391.
[10] Constantinides G, Ravi Chandran KS, Ulm FJ, Van Vliet KJ. Mater Sci Eng A 2006;430:189.
[11] Labour T, Ferry L, Gauthier C, Hajji P, Vigier P. J Appl Polym Sci 1999;74:195.
[12] Shen L, Tjiu WC, Liu T. Polymer 2005;46:11969.
[13] Shen L, Phang IY, Liu T. Polym Test 2006;25:249.
[14] Gourrier A, Garcia-Gutierrez MC, Riekel C. Phil Mag 2006;86:5753.
[15] Du B, Zhang J, Yang Q, He T. Macromolecules 2000;33:7521.
[16] Binnig G, Quate CF, Gerber Ch. Phys Rev Lett 1986;56:930.
[17] Bonnell D. Scanning probe microscopy and spectroscopy. second ed. New York: Wiley-VCH; 2000.
[18] Magonov S. Visualization of polymer structures with atomic force microscopy. In: Bhushan B, Fuchs H, Hosaka S, editors. Applied scanning probe methods. Berlin: Springer Verlag; 2003. p. 207.

[19] Bhushan B. Wear 2001;251:1105.
[20] Clifford CA, Seah MP. Appl Surf Sci 2005;252:1915.
[21] Garcia-Manyes S, Guell AG, Gorostiza P, Sanz F. J Chem Phys 2005;123:114711.
[22] Miake K, Satomi N, Sasaki S. Appl Phys Lett 2006;89:031925.
[23] Silva ECCM, Van Vliet KJ. Nanotechnology 2006;17:5525.
[24] Lin DC, Dimitriadis EK. Trans ASME 2007;129:430.
[25] Tranchida D, Piccarolo S, Soliman M. Macromolecules 2006;39:4547.
[26] Tai K, Dao M, Suresh S, Palazoglu A, Ortiz C. Nat Mater 2007;6:454.
[27] Levy R, Maaloum M. Nanotechnology 2002;13:33.
[28] Burnham NA, Chen X, Hodges CS, Matei GA, Thorensen EJ, Roberts CJ, et al. Nanotechnology 2003;14:1.
[29] Clifford CA, Seah MP. Nanotechnology 2005;16:1660.
[30] Mendels DA, Lowe M, Cuenat A, Cain MG, Vallejio E, Ellis D, et al. J Micromech Microeng 2006;16:1720.
[31] Matei GA, Thorensen EJ, Pratt JR, Newell DB, Burnham NA. Rev Sci Inst 2006;77:1.
[32] Fisher-Cripps AC. Nanoindentation. second ed. Berlin: Springer Verlag; 2004.
[33] Meddad A, Fisa B. J Appl Polym Sci 1996;64:653.
[34] Oliver WC, Pharr GM. J Mater Res 1992;7:1564.
[35] Youn SW, Seo PK, Kang CG. J Mater Proc Technol 2005;162–163:260.
[36] Chudoba T, Richter F. Surf Coat Technol 2001;148:191.
[37] Cheng J, Wang W, Ian LH, Lu K. Scripta Mater 2003;49:645.
[38] Murthy NS, Stamm M, Sibilia JP, Krimm S. Macromolecules 1989;22:1261.
[39] Yu N, Polycarpou AA, Conry TF. Thin Solid Films 2004;450:295.
[40] Tashiro K, Tadokoro H. Macromolecules 1981;14:781.
[41] Lewis ELV, Ward IM. J Macromol Sci Phys B 1981;19:75.
[42] Palabiyik M, Bahadur S. Wear 2000;246:149.
[43] Qin J, Huang Y, Hwang KC, Song J, Pharr GM. Acta Mater 2007;55:6127.
[44] Durst K, Goken M, Vehoff H. J Mater Res 2004;19:85.
[45] Kaji K, Sakurada I. Macromol Chem 1978;179:209.
[46] Dao M, Chollacoop N, Van Vliet KJ, Venkatesh TA, Suresh S. Acta Mater 2001;49:3899.
[47] Cordill MJ, Mook WM, Nair AK, Farkas D, Gerberich WW. JOM 2007;9:59.